8 channel filter design
With improvements to lower interbank

Tom Smy,
Sanam Moslemi Tabriz

Carleton University & Department of Electronics

Abstract: Step by step design of an eight channel filter using ring resonators and waveguide crossings. We also talk about solutions to minimize interbank crosstalk between channels.

Index Terms: Ring resonator, filter, inerband crosstalk, resonant splitting.

1. Theory

Here we studying an eight channel filter using ring resonators and waveguide crossings. There is two types of disruption happening in this circuits;

1) **Resonant splitting**

   This effect happens because of poor filter design where resonant peak and the FWHM of the individual channels interfere with each other, see Fig. **??**. As shown in the Fig. **??** channels 2, 5 and 6 are overlapping. To overcome resonant splitting, we need to properly design the structural parameters of the circuit based on the desired specification; bandwidth, channel's drop wavelength.

Fig. 1. Resonant splitting in the filter

2) **Interbank crosstalk** Interbank crosstalk happens between channels with different wavelength. When a signal in out of bandwidth of a channel but still interfere with the channel performance we experience interbank crosstalk as shown in the Fig. 2. To overcome this issue we need to design High-Q filters with narrower bandwidth.
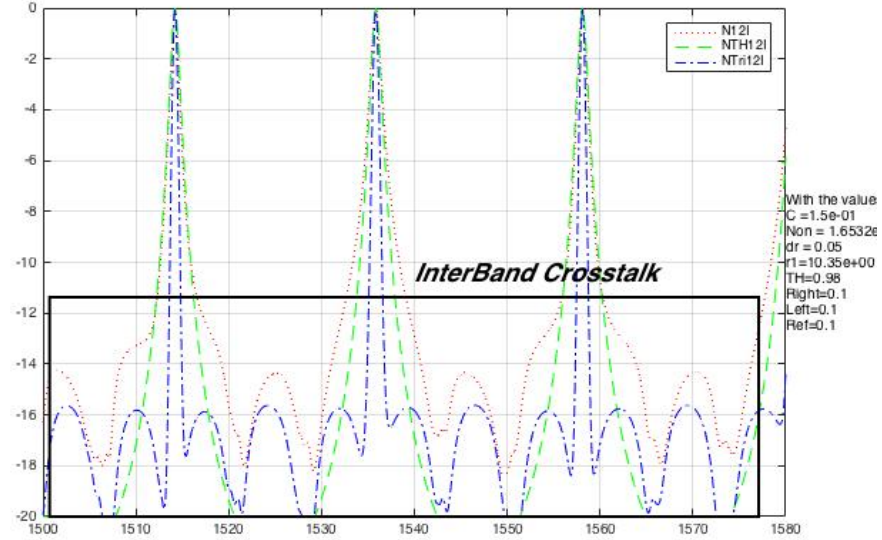

Fig. 2. Interbank crosstalk between channels

2. Design details

The purpose is to design an eight channel filter with equal space between channels and the first channel should resonate at $\lambda_1 = 1529nm$.

$$m\lambda = n_{eff}L \qquad where \; m \; is \; an \; integer \quad and \quad L = 2\pi R. \tag{1}$$

Then for ring 1 (ch1) we have $R_1 = 10.30 \, \mu m$. ($n_{eff} = 1.6532$ REFF(ref17-5-chu-1999).

$$FSR \; = \; \frac{\lambda^2}{n_{eff}L} \tag{2}$$

Equation 2 is only valid if we can ignore the dependency of index of reflection to wavelength. If this is not the case then we need to use n_g which in group index of reflection.

$$\lambda_1^{(k)} = \lambda_1 \; + \; (k-1).FSR \quad where \; k \; is \; an \; integer. \tag{3}$$

$$FSR \; = \; \frac{\lambda^2}{n_g L} \tag{4}$$

where

$$n_g \; = \; n_{eff} - \lambda_0 \frac{\delta n_{eff}}{\delta \lambda} \tag{5}$$

Channels are equally spaced by the value

$$\Delta\lambda = \frac{FSR}{n} \quad where \; n \; is \; the \; number \; of \; channels \tag{6}$$

$$\lambda_n = \lambda_1 + (n-1)\Delta\lambda \quad where \ \lambda_n \ is \ the \ wavelength \ for \ the \ n_{th} \ channel. \tag{7}$$

To overcome the resonant splitting, channel linewidth must be designed in a way that channels don't overlap.

$$FWHM = \frac{\kappa^2\lambda^2}{\pi L n_{eff}} \tag{8}$$

Equation 8 will set the maximum of the coupling coefficient to avoid resonant splitting. On the other hand if coupling coefficient is too low, the the bandwidth will be too narrow, so there will be a trade off in the value of coupling coefficient. Bandwidth spec will define the minimum value of the coupling coefficient. The coupling coefficient has a close relation to the gap between the waveguide and the ring. To have a high κ the gap must be very small, meaning the ring and waveguide must very close to each other and that has some fabrication difficulties.

2.1. examples

3. Experimental Details

The experimental set up is schematically illustrated in A compact $\alpha = 46.9$ nm table top discharge-pumped capillary Ne-like Ar laser occupying only a 1 0.5 m2 footprint on an optical table was used for the recording of the hologram.

3.1. Some Extra Details

Lasing was obtained in the 46.9 nm 3s 1P1 3p 1S0 transition of neon-like Ar by exciting Ar filled alumina capillaries 3.2 mm in diameter with a current pulse having an amplitude of 10% to 90% rise time of first half-cycle duration.

3.1.1. Even more details

The pulse generator consists of a 4 stages Marx generator charged at voltages around 45 kV. The fast current pulse was produced by discharging a water dielectric cylindrical capacitor through a spark gap switch connected in series with the capillary load. The current pulse rapidly compresses the plasma column to achieve a dense and hot filamentary plasma channel where a population inversion is created by strong monopole electron impact excitation of the laser upper level and rapid radiative relaxation of the laser lower level. The water serves as a liquid dielectric for the capacitor and also cools the capillary.

3.1.1.a. A continuous

Flow of Ar is injected in the front of the capillary and an optimum Ar gas pressure of 490 mTorr is maintained in the capillary channel. The EUV laser and the vacuum chamber where the hologram was exposed, are connected via a vacuum manifold that provides differential pumping of the chamber that is maintained at 10-5 Torr. The laser, operated with 18.4 cm long capillaries, produces 0.1J pulses at a repetition rate of 1 Hz 15. The high temporal and spatial

$$x = \sum_{1=0}^{z} 2^1 Q \tag{9}$$

coherence of the EUV table top laser permits the recording of large NA holograms for high resolution holographic imaging 18. The test object used in the holographic volume imaging experiment consisted of a tilted metallic surface covered with opaque spherical objects as can be seen in (9). This test object was fabricated placing a 100 nm thick aluminum foil covering a hole 1.5 mm in diameter made in a 80 m thick mylar sheet. The hole was partially covered with a second mylar sheet 80 m thick, as schematically indicated in Fig. **??**.

Humanoid robots have received much attention recently. Although they are able to walk without falling, their movements are not natural looking. In order for these robots to move more like

humans, two technological obstacles need to be addressed: Firstly, there is a lack of flexibility in their body torsos. In all human activities, movements from the spine are involved. Yet, this important factor has been neglected by the majority of humanoid robotic researchers. One of the main reasons is that the added degrees of freedom (DOF) make it more costly and difficult to build a robot. Another key issue is that it is very difficult to program these types of robots so that they can maintain balance. This numerical sectioning technique for holography is verified to produce a robust three dimension image of a test object. This numerical sectioning technique for holography is verified to produce a robust three dimension image of a test object. This numerical sectioning technique for holography is verified to produce a robust three dimension image of a test object.

$$Z = x_1 + x_2 + x_3 + x_4 + x_5 + x_6$$
$$+a + b \tag{10}$$
$$+a + b \tag{11}$$
$$+ a + b \tag{12}$$
$$+ a + b \tag{13}$$

In order to address the above technological challenges, we need to develop flexible spine humanoid robots as experimental platforms. Recently, a few researchers have developed several spinal robots based on the anatomy of the human skeleton, Mizuuchi built a tendon-driven robot called "Kenta" [?], [?]. Although the robot has a spine, there has been no data to show that it can move in a flexible way. Also, the robot cannot stand up without external support because the upper body is too heavy [?]. Mizuuchi later improved his prototype. However, it is also unable to stand up without external support [?], [?].

At the German Space Agency (DLR), Hirzinger and his group developed a spine robot called "Justin". The robot has a 3-DOF movable upper-torso, two arms and dexterous hands. Unlike the tendon-based robots developed by Mizuuchi and his colleagues, each controllable spinal joint of Justin is directly actuated by a DC Motor via a Harmonic Drive Gear. In order to prevent the robot from falling, the designers fixed the robot to a large platform [?]. In November, 2007, researchers from Sugano Lab of Waseda University announced a new humanoid robot for household work and home care. The robot is called "Twendy-One". It has a 4-DOF spine but it is fixed on a wheeled mobile platform. Thus, balancing is not an issue for this robot. It has a 4-DOF spine but it is fixed on a wheeled mobile platform. Thus, balancing is not an issue for this robot.

Inspired by the flexibility of belly dancers, Or conducted the first scientific study on belly dancing [?]. He developed a database of belly dancing movements using computer animations. Later, Or recorded the movements of a professional belly dancer using a 12-camera VICON [?] motion capture system. By analyzing the movements of the dancer, he developed a spinal mechanism which allows a full-body humanoid robot to exhibit all the human spine motions in 3D although with less degree of freedom [?]. Moreover, the robot is able to stand up while performing dynamic torso motions without external support. In terms of controlling the mechanical spine, Or used a model of the lamprey central pattern generator. Experimental results showed that by using such neural networks, only three control parameters are needed to generate all human spinal motions. In order to conduct research on human-robot interactions, Or developed a new, full-body flexible spine humanoid robot [?], [?]. Experimental results showed that it is possible for humans to perceive emotions expressed by a flexible spine humanoid robot. Later, Or developed the world's first humanoid robot that can walk more naturally, like a human, with flexible spinal motions.

The aluminum foil contours over the semicircular aperture to produce a variable height surface with the desirable characteristics for this test in Table I. The 100 nm aluminum foil has a transmission of approximately 35% at $\alpha = 46.9$ nm considering the layer of native oxide 19 and effectively cuts the lower photon energy plasma emission from the Ar discharge in the laser source. The sample was immersed in a solution of MIBK-methyl isobutyl ketone (4-Methyl-2- Pentanone) with

TABLE I
MATH SPACINGS USED BY LaTeX

Size	Width	Cmd.	Used for	Example
small	1/6 em	\,	symbols	ab
medium	2/9 em	\:	binary operators	$a + b$
large	5/18 em	\;	relational operators	$a = b$
negative small	$-1/6$ em	\!	misc. uses	ab

IPA (isopropyl alcohol) 1:3 for 30 seconds, rinsed with IPA for 30 seconds, and was finally dried using compressed nitrogen $x = \sum_{1=0}^{z} 2^1 Q$.

4. Results

We adjusted the[1] exposure so that the photoresist operated in a linear response regime. With exposure by the EUV laser, the holographic interference pattern generated by the reference and the object beams was recorded in the photoresist and converted to a surface modulation after the development. Thus, the holograms were recorded as a relief pattern in the surface of a photoresist deposited on a Si wafer.

- Weight parameters for the simulated robot.
- Length of each body link.
- Specifications of body joints. Upper Torso means the spine. Due to symmetry, body parts from the right are not shown.
- Neuron parameters. Θ is the threshold, Γ is the gain. τ_D and τ_A are respectively the time constant of the dendritic sums and that of the frequency adaptation. μ is the coefficient of frequency adaptation.

Holograms recorded in such a fashion can not be reconstructed in the conventional way with an optical reconstruction beam. In order to numerically reconstruct the holograms, the surface modulation was digitized with a Novascan atomic force microscope (AFM) operated in tapping mode. Holograms recorded in such a fashion can not be reconstructed in the conventional way with an optical reconstruction beam. In order to numerically reconstruct the holograms, the surface modulation was digitized with a Novascan atomic force microscope (AFM) operated in tapping mode.

1) Screenshot of the Webots simulation environment.
2) Schematic diagram of the simulated robot.
3) Schematic of the model lamprey CPG. Connections with a dot ending represent inhibitory connections while those with an arrow ending represent excitatory connections.
4) Sample output of a segmental oscillator (the 20th segment from the CPG). MNl and MNr respectively represents the output from the left and right motoneurons. Note the regularity of the neural pulses.

Two holograms digitized in this manner are displayed in Fig. **??**. The digital reconstruction of the hologram digitized by the AFM is based on a numerical Fresnel propagator in Table II and III. To obtain the amplitude and the phase distribution of the field in the image plane, the field emerging from the hologram illuminated by a plane wave is back propagated with the Fresnel-Kirchhoff integral. The integral was evaluated by the product of the spatial frequency representation of the

---

[1]The aluminum foil contours over the semicircular aperture to produce a variable height surface with the desirable characteristics for this test. The 100 nm aluminum foil has a transmission of approximately 35% at $\alpha = 46.9$ nm considering the layer of native oxide 19 and effectively cuts the lower photon energy plasma emission from the Ar discharge in the laser source.

TABLE II
POSSIBLE Ω FUNCTIONS

Range	$\Omega(m)$
$x < 0$	$\Omega(m) = \displaystyle\sum_{i=0}^{m} K^{-i}$
$x \geq 0$	$\Omega(m) = \sqrt{m}$

TABLE III
NETWORK DELAY AS A FUNCTION OF LOAD

β	Average Delay	
	λ_{min}	λ_{max}
1	0.057	0.172
10	0.124	0.536
100	0.830	0.905[*]

[*]limited usability

hologram obtained through a two dimensional fast Fourier transformation and the quadratic phase free space Fresnel propagator in the spatial frequency domain.

Theorem 1 (Einstein-Podolsky-Rosenberg):
The back-propagation distance is determined by calculating the Fresnel zone plate (FZP) focal distance for the specific hologram geometry. For the specific geometry employed in this experiment, the FZP focal length is approximately the distance between the object and the recording medium. The digital images of the holograms processed with the Fresnel propagation code generated the reconstructed images shown in Fig. **??**.

Holograms recorded in such a fashion can not be reconstructed in the conventional way with an optical reconstruction beam. In order to numerically reconstruct the holograms, the surface modulation was digitized with a Novascan atomic force microscope operated in tapping mode.

Lemma 1:
The back-propagation distance is determined by calculating the Fresnel zone plate (FZP) focal distance for the specific hologram geometry For the specific geometry employed in this experiment, the FZP focal length is approximately the distance between the object and the recording medium. The digital images of the holograms processed with the Fresnel propagation code generated the reconstructed images shown in Fig. **??**.

Holograms recorded in such a fashion can not be reconstructed in the conventional way with an optical reconstruction beam. In order to numerically reconstruct the holograms.

Proof:
The back-propagation distance is determined by calculating the Fresnel zone plate (FZP) focal distance for the specific hologram geometry. For the specific geometry employed in this experiment, the FZP focal length is approximately the distance between the object and the recording medium. The digital images of the holograms processed with the Fresnel propagation code generated the reconstructed images shown in Fig. **??**. ∎

5. Conclusions

We have demonstrated that through detailed processing of the reconstructed holographic images, performed by changing the object-hologram distance in the reconstruction code, it is possible to discriminate depth in the object. Using a specially fabricated object composed of spherical markers 465 nm in diameter spread on a tilted transparent surface, the reconstruction and analysis of the hologram allowed to map the surface topography with a resolution close to 2 m, with such resolution depending on the particular NA of the exposure.

The lateral resolution of the image obtained by numerical reconstruction was assessed utilizing a wavelet image decomposition and image correlation. The best lateral resolution obtained with a high NA recording, 164 nm, represents an improvement of more than a factor two relative to previously published results.

Acknowledgements